

## Electronic Supplementary Information (ESI)

### Negative-pressure sulfurization of antimony sulfide thin films for generating record open-circuit voltage of 805 mV in solar cell applications

Xiaoqi Peng,<sup>#ab</sup> Junjie Yang,<sup>#ab</sup> Qi Zhao,<sup>ab</sup> Huihui Gao,<sup>ab</sup> Yuqian Huang,<sup>ab</sup> Haolin Wang,<sup>ab</sup> Changfei Zhu,<sup>ab</sup> Rongfeng Tang,<sup>\*ab</sup> and Tao Chen<sup>\*ab</sup>

- a. Hefei National Research Center for Physical Sciences at the Microscale, CAS Key Laboratory of Materials for Energy Conversion, Department of Materials Science and Engineering, School of Chemistry and Materials Science, University of Science and Technology of China, Hefei, 230026, China.
- b. Institute of Energy, Hefei Comprehensive National Science Center, Hefei, 230051, China.

\*Corresponding authors: Rongfeng Tang, Tao Chen

E-mail: [rftang@ustc.edu.cn](mailto:rftang@ustc.edu.cn), [tchenmse@ustc.edu.cn](mailto:tchenmse@ustc.edu.cn)

# These authors contributed equally to this work.

#### **This file includes:**

Supplementary note S1 to S2

Figure S1 to S10

Table S1 to S4

References

## Supplementary Note

### Note 1

#### Principles of Deep-level Transient Spectroscopy

We conducted deep-level transient spectroscopy (DLTS) to detect the deep-level defects properties and the defect level is identified from DLTS signal using Fourier deconvolution algorithm. The active energy ( $E_a$ ,  $E_C - E_T$  or  $E_T - E_V$ ) and capture cross section of electron traps and hole traps can be calculated by the Arrhenius Equations (1) and (2),

$$\ln(\tau_e v_{th,p} N_V) = \frac{E_T - E_V}{k_B} \frac{1}{T} - \ln(X_p \sigma_p) \#(1)$$

$$\ln(\tau_e v_{th,n} N_C) = \frac{E_C - E_T}{k_B} \frac{1}{T} - \ln(X_n \sigma_n) \#(2)$$

where  $\tau_e$ ,  $N_V$ ,  $N_C$ ,  $E_T$ ,  $E_V$ , and  $E_C$  are emission time constant, valence band state density, conduction band state density, trap energy level, valence band, and conduction band, respectively.  $v_{th,n/p}$ ,  $X_{n/p}$ , and  $\sigma_{n/p}$  are thermal velocity, entropy factor, and capture cross-section for electron and hole, respectively.  $E_a$  can be obtained from the slope of the corresponding line, and the  $\sigma$  can be obtained from the y-intercept of the lines. The trap concentration ( $N_T$ ) can be acquired from Equation (3):

$$N_T = 2N_S \frac{\Delta C}{C_R} \#(3)$$

where  $N_S$  is the shallow donor concentration,  $C_R$  is the capacitance under reverse bias, while  $\Delta C$  represents the amplitude of transient capacitance.

The product of the capture cross section and the defect density ( $\sigma \times N_T$ ) is considered as an important parameter for the intuitive evaluation of the carrier lifetime, and the relationship follows the following Equation (4):

$$\tau_{trap} = \frac{1}{v \sigma N_T} \#(4)$$

where  $v$  is the thermal velocity of electric charge.<sup>1, 2</sup>

## Note 2

### Calculation of Texture Coefficient

The preferred orientation of the film can generally be described qualitatively by texture coefficient (TC). According to the previous work,<sup>3</sup> the calculation of TC for a given crystal planes for our  $\text{Sb}_2\text{S}_3$  film is based on the following Equation (5) :

$$TC_{hkl} = \frac{I_{(hkl)}}{I_{0(hkl)}} / \left( \frac{1}{N} \sum_{i=1}^N \frac{I_{(h_i k_i l_i)}}{I_{0(h_i k_i l_i)}} \right) \#(5)$$

where  $I_{(hkl)}$  is the diffraction peak intensity of (hkl) plane in the measured XRD pattern, while  $I_{0(hkl)}$  is the diffraction peak intensity of (hkl) plane in the standard XRD pattern (for  $\text{Sb}_2\text{S}_3$  film, JCPDS 42-1393) and N is the number of Prague reflections considered. The larger TC indicates the preferred orientation on the crystal plane, and the TC greater than 1 indicates the preferred orientation.

In our work, we have selected five main (hk1) plans and five main (hk0) plans to be included in the calculation of texture coefficient, which are respectively (120), (220), (130), (320), (240), (101), (111), (211), (221), and (301). So here, the value of N is 10. The specific calculation results are shown in the table below. It can be seen from the data in the table that compared with the reference  $\text{Sb}_2\text{S}_3$ -HP, the film of  $\text{Sb}_2\text{S}_3$ -S-TF shows a higher  $TC_{(hk1)}$  and a lower  $TC_{(hk0)}$ , which indicates that the grain growth in the film is dominated by vertical growth and has better charge transport capability.

	$\text{Sb}_2\text{S}_3$ -HP	$\text{Sb}_2\text{S}_3$ -TF	$\text{Sb}_2\text{S}_3$ -S-TF	$\text{Sb}_2\text{S}_3$ -HP-TF
$TC_{(120)}$	1.07707	0.81729	0.66133	1.10156
$TC_{(220)}$	1.63687	1.39281	0.89967	1.73101

$TC_{(130)}$	0.86199	0.90851	0.74806	0.94287
$TC_{(320)}$	1.53940	1.33592	0.95887	1.69432
$TC_{(240)}$	1.22544	0.75690	0.58817	1.34318
$TC_{(101)}$	0.37954	0.73215	0.79005	0.33497
$TC_{(111)}$	0.45793	0.82540	1.14163	0.50819
$TC_{(211)}$	0.47821	0.83663	0.98007	1.46801
$TC_{(221)}$	0.67871	0.89138	0.98214	0.63334
$TC_{(301)}$	1.66483	1.50301	2.25002	1.24255

## Supplementary Figure

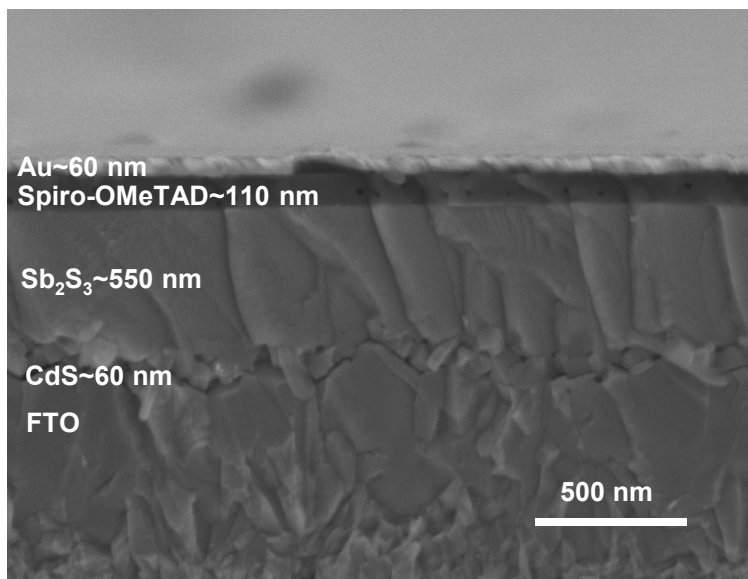


Fig. S1. Cross section SEM image of the full device

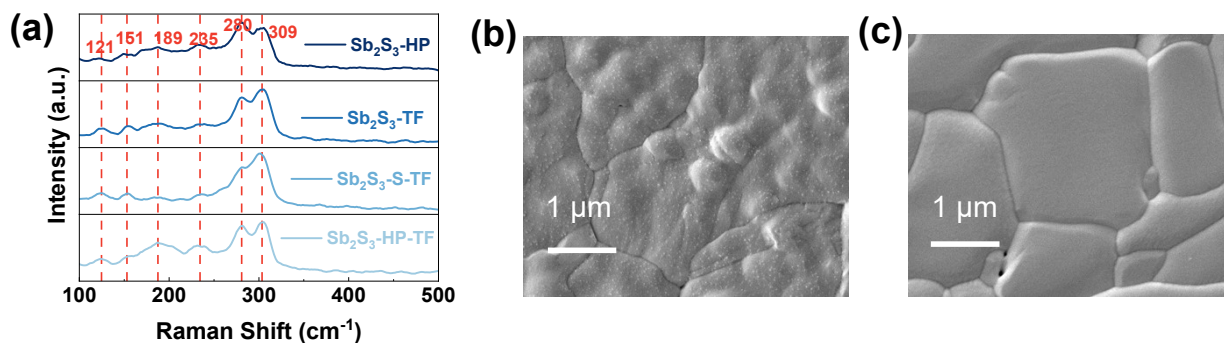
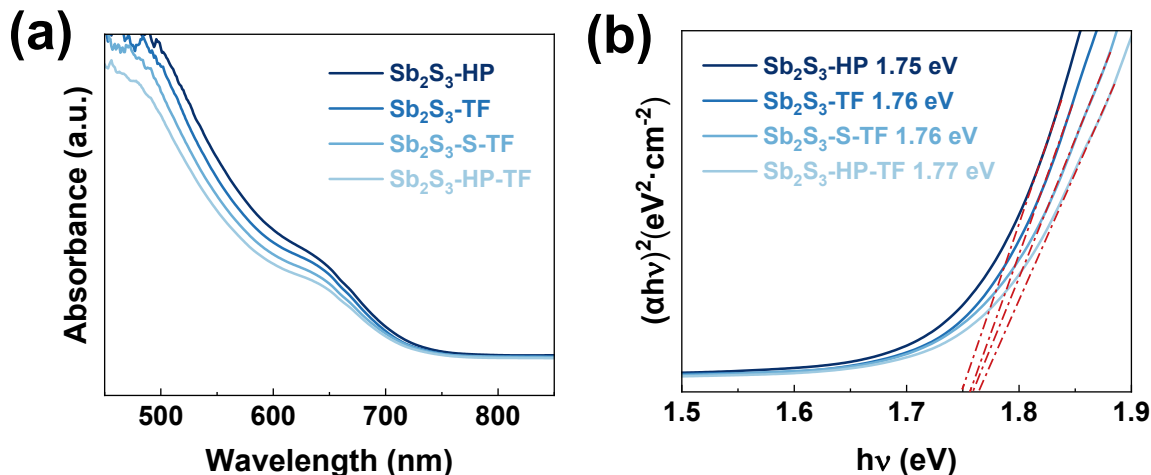


Fig. S2. Characterization of structure and surface morphology of the films. (a) Raman spectra of  $Sb_2S_3$ -HP,  $Sb_2S_3$ -TF,  $Sb_2S_3$ -S-TF, and  $Sb_2S_3$ -HP-TF films. The surface SEM morphologies of films, (b)  $Sb_2S_3$ -TF and (c)  $Sb_2S_3$ -HP-TF.

The Raman spectras of  $Sb_2S_3$ -HP,  $Sb_2S_3$ -TF,  $Sb_2S_3$ -S-TF, and  $Sb_2S_3$ -HP-TF are shown in Fig. S2. The peaks at position of 121  $cm^{-1}$ , 151  $cm^{-1}$ , 189  $cm^{-1}$ , 235  $cm^{-1}$ , 280  $cm^{-1}$ , and 309  $cm^{-1}$  in the four samples are all from  $Sb_2S_3$ .<sup>4</sup> In specific, the peaks at 189  $cm^{-1}$  and 235  $cm^{-1}$  belong to the asymmetric and symmetric bending vibration of S-Sb bond, respectively, while 280  $cm^{-1}$  and 309  $cm^{-1}$  can be assigned to the asymmetric and symmetric tensile vibration of S-Sb bond. The above

four peaks indicates S and Sb interact in the  $A_g$  modes, while the appearance of peaks located around  $121\text{ cm}^{-1}$  and  $151\text{ cm}^{-1}$  indicates good crystallinity of  $\text{Sb}_2\text{S}_3$ .<sup>5</sup>



**Fig. S3. UV-visible absorption characterization of the films.** (a) UV-vis absorption spectrum of the films. (b) Tauc plots of  $(\alpha h\nu)^2$  versus  $h\nu$ . The direct band gap  $E_g$  are calculated according to the equation of  $(\alpha h\nu)^2 = A (h\nu - E_g)$ , where  $\alpha$  is the absorption coefficient,  $h$  is the planck constant,  $\nu$  is the frequency of the incident photon, and  $A$  is a proportionality constant.

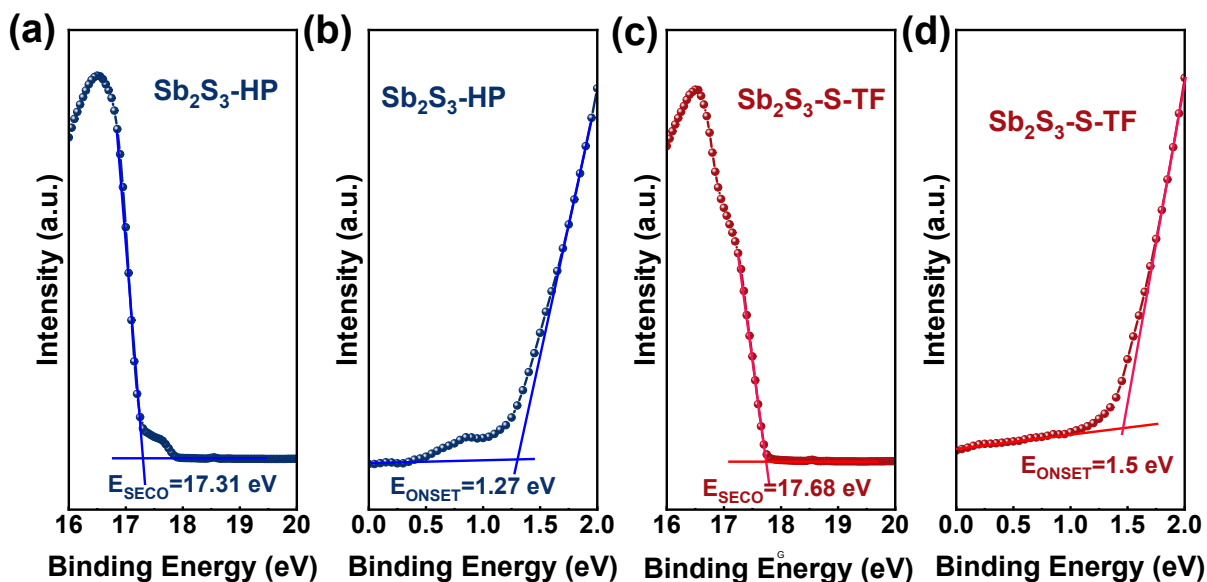


**Fig. S4. Ultraviolet Photoelectron Spectroscopy spectra. (a)  $\text{Sb}_2\text{S}_3$ -HP, (b)  $\text{Sb}_2\text{S}_3$ -S-TF. Valance band spectra of (c)  $\text{Sb}_2\text{S}_3$ -HP, (d)  $\text{Sb}_2\text{S}_3$ -S-TF.**

The conduction band position ( $E_C$ ), valence band position ( $E_V$ ), Fermi energy level ( $E_F$ ), and work function ( $\Phi$ ) of the films can be obtained from the UV-vis and UPS results according to the following equations:

$$\Phi = |E_{SECO} - 21.22 \text{ eV (Ultraviolet photon energy)}| \#(6)$$

$$E_V = -|\Phi + E_{ONSET}| \#(7)$$

$$E_C = E_V + E_g \#(8)$$

where  $E_{SECO}$  is defined as the secondary electron cut off, and  $E_{ONSET}$  refers to the maximum valence band, while  $\Phi$  represents the work function, and is defined as the difference between  $E_F$  and vacuum energy level.

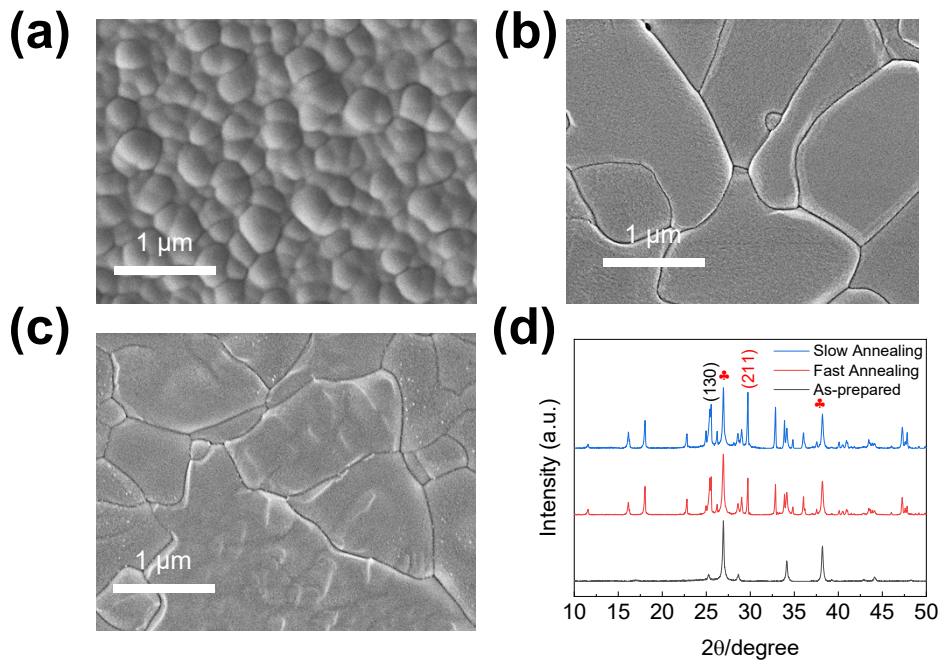


**Fig. S5. Characterization of surface morphology and structure of the films. SEM images of (a) the as-prepared  $\text{Sb}_2\text{S}_3$  precursor films, (b)  $\text{Sb}_2\text{S}_3$  crystalline films obtained through rapid**

thermal annealing on hot plate in glove box for 30 mins, (c) the film obtained through slow thermal annealing on hot plate in glove box (the heating time from room temperature to 350 °C is 20 mins and the holding time is 10 mins). (d) XRD patterns of the corresponding films.

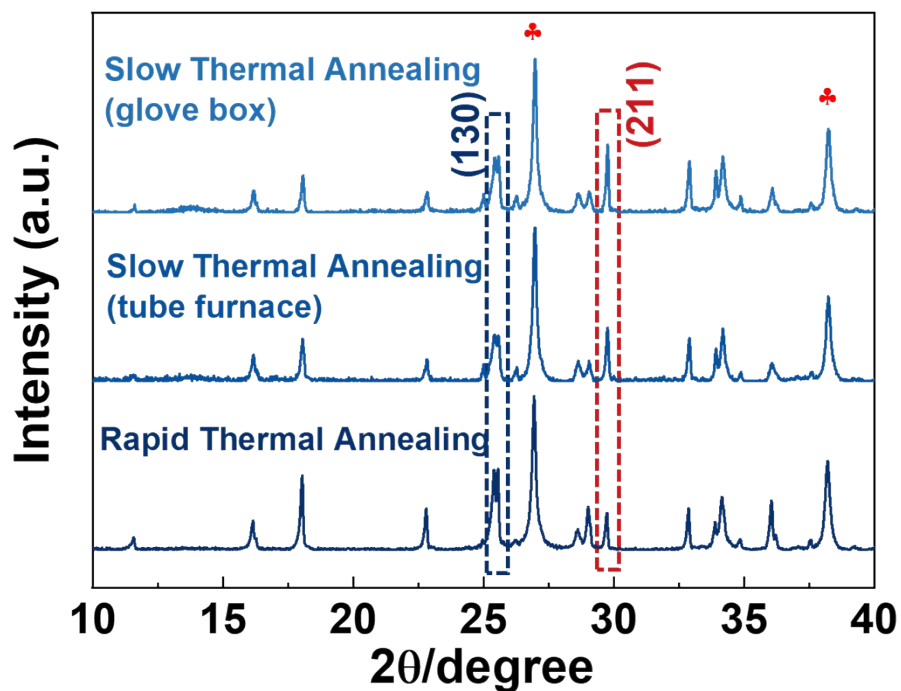


**Fig. S6. XRD characterization.** XRD patterns of  $\text{Sb}_2\text{S}_3$  films obtained by process of rapid thermal annealing, slow annealing on hot plate in glove box and slow annealing in tube furnace, respectively.

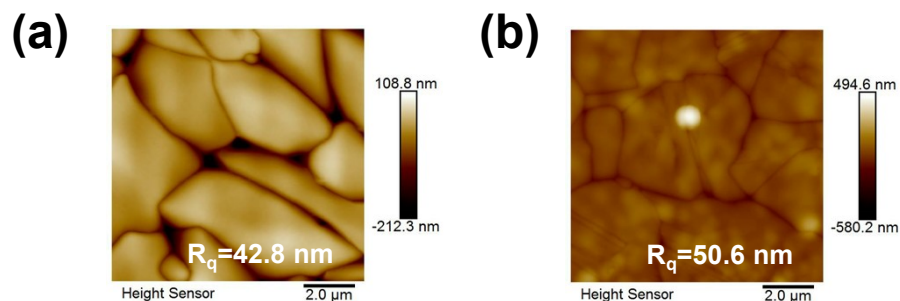


**Fig. S7. AFM images of the films.** (a)  $\text{Sb}_2\text{S}_3$ -HT ( $R_q=42.8$  nm), (b)  $\text{Sb}_2\text{S}_3$ -S-TF ( $R_q=50.6$  nm).

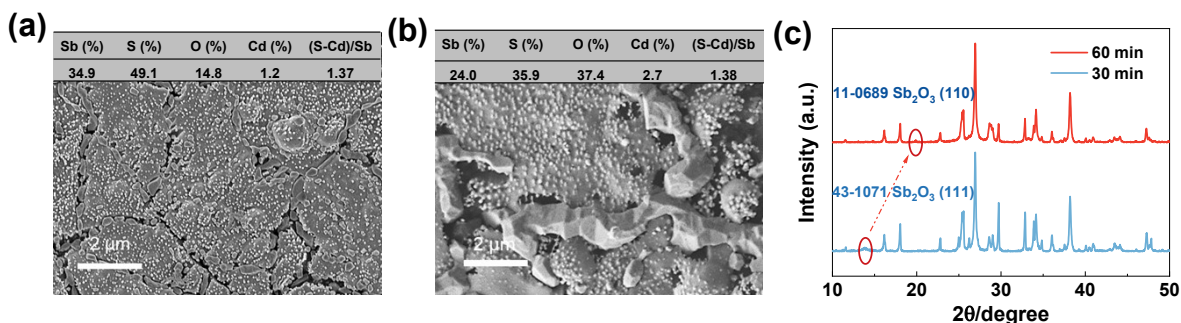


**Fig. S8. SEM images of the films.** SEM images of the surface morphology of  $Sb_2S_3$  films annealed slowly in glove box for **(a)** 30 mins, and **(b)** 60 mins, and with a heating time controlled at 20 mins. **(c)** XRD patterns of the corresponding films.

We further prolonged the annealing time to 30 mins and 60 mins (Fig. S8). The morphology of the obtained two films exhibit significant changes, with a significant increase of the tiny particles on the film surface, and an increase in the content of oxygen element detected by EDS. Furthermore, new peaks appear in the XRD pattern of the two films obtained after 30 mins and 60 mins of annealing treatment. The peak at  $13.34^\circ$  in the former belongs to (111) of  $Sb_2O_3$  phase, while the peak at  $20.12^\circ$  in the latter belongs to (110) of  $Sb_2O_3$  phase.

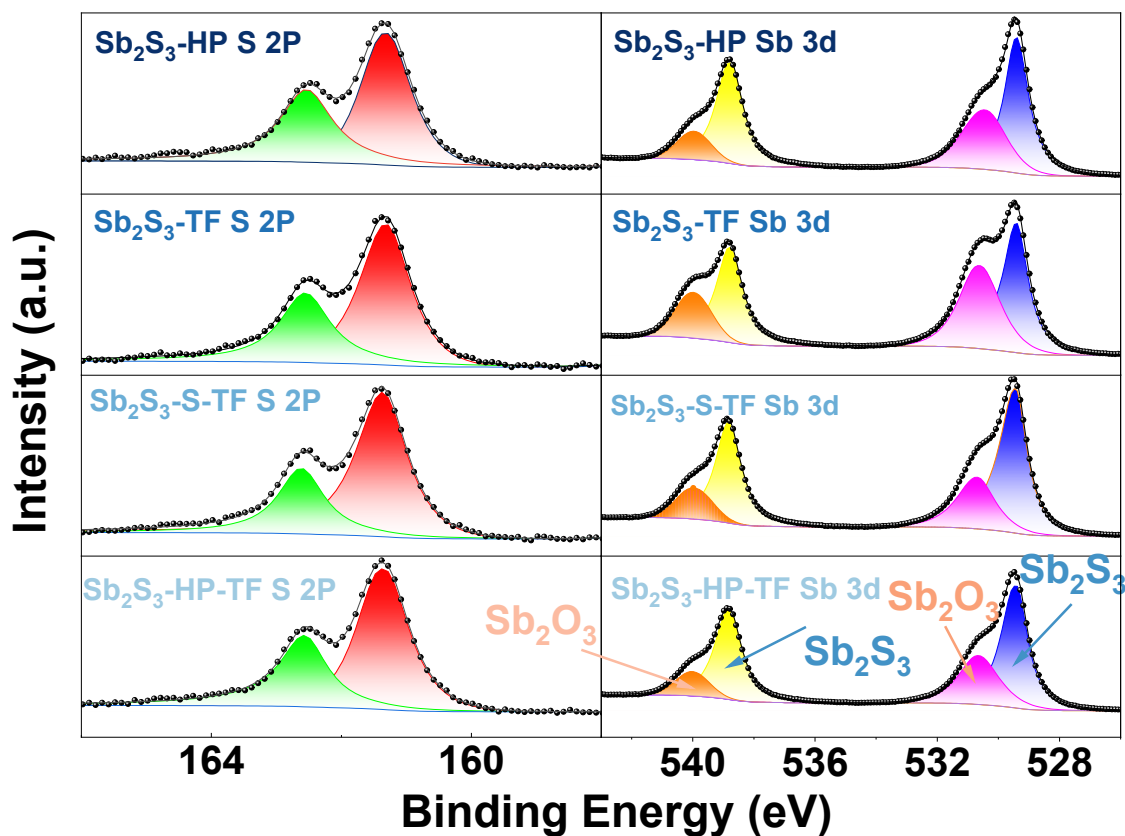
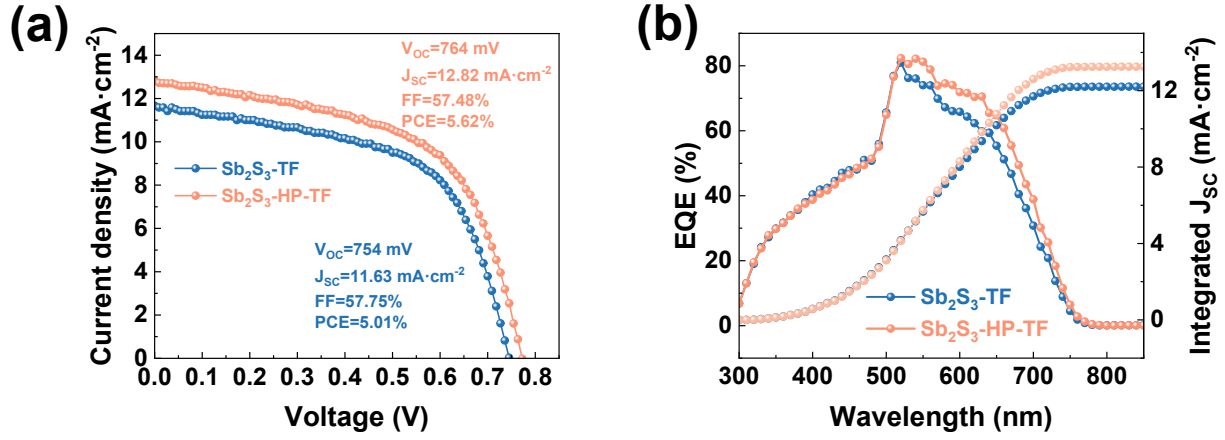


Fig. S9. High-resolution XPS spectra of S 2p and Sb 3d for  $\text{Sb}_2\text{S}_3$ -HP,  $\text{Sb}_2\text{S}_3$ -TF,  $\text{Sb}_2\text{S}_3$ -S-TF, and  $\text{Sb}_2\text{S}_3$ -HP-TF films.

Through X-ray Photoelectron Spectroscopy (XPS), we analyzed the chemical composition and elemental valence states of the films. The high-resolution core spectra of S 2p and Sb 3d are shown in Fig. S9, and the binding energy of the corresponding separated peaks are listed in table S3. Specifically, the two peaks with binding energy around 161.32 eV and 162.55 eV belong to the S  $2p_{3/2}$  and S  $2p_{1/2}$ , while the peaks with binding energy around 529.41 eV and 538.80 eV can be attributed to Sb  $3d_{5/2}$  and Sb  $3d_{3/2}$  of  $\text{Sb}^{3+}$  that bond with  $\text{S}^{2-}$  in  $\text{Sb}_2\text{S}_3$ . However, the separated peaks at position of around 530.65 eV and 539.90 eV originates from  $\text{Sb}_2\text{O}_3$ . Furthermore, the  $\text{Sb}_2\text{S}_3$ -TF film shows the highest content of  $\text{Sb}_2\text{O}_3$  due to the long heat treatment time. In  $\text{Sb}_2\text{S}_3$ -S-

TF film, the content of  $\text{Sb}_2\text{O}_3$  is significantly reduced, and the detected  $\text{Sb}_2\text{O}_3$  is mainly caused by the inevitable adsorption of oxygen in the air.



**Fig. S10. Photovoltaic performance of the devices.** (a)  $J$ - $V$  curves of the solar cells based on  $\text{Sb}_2\text{S}_3$ -TF and  $\text{Sb}_2\text{S}_3$ -HP-TF. (b) The corresponding EQE spectra of the devices.

### Supplementary Table

**Table S1. The ratio of  $V_{OC}$ ,  $J_{SC}$ , FF, and PCE to the corresponding S-Q limit value for the current best devices based on planar- and sensitized-structure antimony sulfide solar cells<sup>2, 6, 7</sup>.**

Materials	Types		$V_{OC}$ (V)	$J_{SC}$ (mA cm <sup>-2</sup> )	FF (%)	PCE (%)
			<b>Sb<sub>2</sub>S<sub>3</sub></b> <b>(1.68 eV)</b>	<b>Planar</b>	<b>Champion</b>	0.757
<b>S-Q limit</b>	1.398	23.06			90.87	29.28
<b>Champion/ S-Q</b>	<b>54.1%</b>	<b>75.5%</b>			<b>66.6%</b>	<b>27.3%</b>
<b>Mesoporous</b>	<b>Champion</b>	0.711		16.10	65.00	7.50
	<b>S-Q limit</b>	1.398		23.06	90.87	29.28
	<b>Champion/ S-Q</b>	<b>50.9%</b>		<b>69.8%</b>	<b>71.5%</b>	<b>25.6%</b>

**Table S2. EDS results of the films.**

Films	Sb (%)	S (%)	Cd (%)	(S-Cd)/Sb
<b>Sb<sub>2</sub>S<sub>3</sub>-HP</b>	36.8	58.5	4.7	1.462
<b>Sb<sub>2</sub>S<sub>3</sub>-TF</b>	36.4	58.1	5.5	1.444
<b>Sb<sub>2</sub>S<sub>3</sub>-S-TF</b>	37.8	59.7	2.5	1.513
<b>Sb<sub>2</sub>S<sub>3</sub>-HP-TF</b>	39.4	59.4	1.2	1.477

**Table S3. Binding energies of the separated S2p and Sb3d XPS peaks in the Sb<sub>2</sub>S<sub>3</sub>-HP, Sb<sub>2</sub>S<sub>3</sub>-TF, Sb<sub>2</sub>S<sub>3</sub>-S-TF, and Sb<sub>2</sub>S<sub>3</sub>-HP-TF films.**

Films	S 2P		Sb 3d				
	S 2P <sub>3/2</sub>	S 2P <sub>1/2</sub>	Sb-S 3d <sub>5/2</sub>	Sb-O 3d <sub>5/2</sub>	Sb-S 3d <sub>3/2</sub>	Sb-O 3d <sub>3/2</sub>	Sb <sub>2</sub> O <sub>3</sub> / Sb <sub>2</sub> S <sub>3</sub>
<b>Sb<sub>2</sub>S<sub>3</sub>-HP</b>	161.30	162.54	529.41	530.44	538.76	539.96	0.483
<b>Sb<sub>2</sub>S<sub>3</sub>-TF</b>	161.32	162.55	529.41	530.65	538.80	539.98	0.643
<b>Sb<sub>2</sub>S<sub>3</sub>-S-TF</b>	161.37	162.62	529.44	530.69	538.84	539.93	0.388
<b>Sb<sub>2</sub>S<sub>3</sub>-HP-TF</b>	161.34	162.58	529.41	530.64	538.79	540.01	0.417

**Table S4. Five main optimization parameters involved in the sulfurization process.**

Photovoltaic performance of the devices based on the films obtained in the following conditions: with or without post-annealing, different weights of sulfur powder, different sulfurization time, different sulfurization temperature, and the distance between sulfur powder and the substrate.

Post-annealing	$V_{OC}$ (mV)	$J_{SC}$ (mA cm <sup>-2</sup> )	FF (%)	PCE (%)
<b>without</b>	724	10.59	54.26	4.16
<b>with</b>	802	12.67	61.23	6.22

Weight of sulfur powder (g)	$V_{OC}$ (mV)	$J_{SC}$ (mA cm <sup>-2</sup> )	FF (%)	PCE (%)
<b>0.025</b>	754	12.09	58.04	5.29
<b>0.050</b>	811	11.65	63.04	5.96
<b>0.100</b>	792	12.06	63.88	6.11
<b>0.200</b>	782	12.06	56.77	5.35

Sulfurization time (mins)	$V_{OC}$ (mV)	$J_{SC}$ (mA cm <sup>-2</sup> )	FF (%)	PCE (%)
<b>5</b>	782	10.05	53.88	4.24
<b>10</b>	792	12.69	63.77	6.41

<b>15</b>	773	12.21	65.26	6.16
<b>20</b>	754	12.52	58.61	5.53

<b>Sulfurization temperature (°C)</b>	$V_{OC}$ (mV)	$J_{SC}$ (mA cm <sup>-2</sup> )	FF (%)	PCE (%)
<b>350</b>	734	11.53	49.64	4.20
<b>360</b>	773	11.56	65.40	5.85
<b>370</b>	802	12.18	63.26	6.18
<b>380</b>	791	11.94	58.31	5.51

<b>Distance between sulfur powder and substrate (cm)</b>	$V_{OC}$ (mV)	$J_{SC}$ (mA cm <sup>-2</sup> )	FF (%)	PCE (%)
<b>6</b>	699	9.52	50.21	3.34
<b>8</b>	782	12.20	60.41	5.76
<b>10</b>	791	12.80	62.12	6.29
<b>12</b>	773	12.34	59.26	5.65

The optimal sulfurization condition we ultimately used was 0.1 g of sulfur powder, and sulfurized at 370 °C for 10 mins. The distance between the sulfur powder and the substrate was controlled at 10 cm, but no further post-annealing treatment was required.

## References

1. Y. Zhao, S. Wang, C. Li, B. Che, X. Chen, H. Chen, R. Tang, X. Wang, G. Chen, T. Wang, J. Gong, T. Chen, X. Xiao and J. Li, *Energy & Environmental Science*, 2022, **15**, 5118-5128.
2. S. Wang, Y. Zhao, B. Che, C. Li, X. Chen, R. Tang, J. Gong, X. Wang, G. Chen, T. Chen, J. Li and X. Xiao, *Adv Mater*, 2022, **34**, e2206242.
3. R. Tang, X. Wang, W. Lian, J. Huang, Q. Wei, M. Huang, Y. Yin, C. Jiang, S. Yang, G. Xing, S. Chen, C. Zhu, X. Hao, M. A. Green and T. Chen, *Nature Energy*, 2020, **5**, 587-595.
4. W. Lian, C. Jiang, Y. Yin, R. Tang, G. Li, L. Zhang, B. Che and T. Chen, *Nat Commun*,

- 2021, **12**, 3260.
5. R. Parize, T. Cossuet, O. Chaix-Pluchery, H. Roussel, E. Appert and V. Consonni, *Mater Design*, 2017, **121**, 1-10.
  6. Y. C. Choi, D. U. Lee, J. H. Noh, E. K. Kim and S. I. Seok, *Advanced Functional Materials*, 2014, **24**, 3587-3592.
  7. C. Chen and J. Tang, *Acs Energy Lett*, 2020, **5**, 2294-2304.